

Tunable contributions from rectification and momentum transfer to 1D Coulomb Drag

Mingyang Zheng,¹ Rebika Makaju,¹ Rasul Gazizulin,^{1,2} Sadhvikas J. Addamane,³ and D. Laroche^{1,*}

¹*Department of Physics, University of Florida, Gainesville, FL 32611, USA*

²*National High Magnetic Field Laboratory High B/T Facility,
University of Florida, Gainesville, 32611, FL, USA*

³*Center for Integrated Nanotechnologies, Sandia National Laboratories, Albuquerque, NM 87185, USA*

Coulomb drag is a powerful tool to study interactions in coupled low-dimensional systems. Historically, Coulomb drag has been attributed to a frictional force arising from momentum transfer whose direction is dictated by the current flow. However recent findings in one-dimensional systems have also identified a rectified contribution that is independent of the current flow direction. In this work, we present Coulomb drag measurements between vertically coupled GaAs/AlGaAs quantum wires separated vertically by a hard barrier only 15 nm wide where both momentum transfer and rectified Coulomb drag signals are observed simultaneously, and whose relative magnitude are temperature and gate tunable. Our study opens up the possibility of studying the physical mechanisms behind the onset of both momentum transfer and charge rectification drag simultaneously in a single device, ultimately leading to a better understanding of Luttinger liquids in multi-channel wires and paving the way for the creation of energy harvesting devices.

Keywords: Coulomb Drag, Luttinger Liquid, Quantum wires, Low temperature, Energy rectification

I. Introduction

In recent years, there has been a renewed interest in the study of one-dimensional systems (1D), owing to their potential for hosting topologically protected Majorana-Bound-States [1, 2] and for realizing heat harvesting devices [3, 4]. Indeed, due to the strong electron-electron interactions arising from the significantly reduced screening [5, 6], 1D systems are a rich platform for the observation of exotic quantum phases and states. The Tomonaga Luttinger liquid (TLL) framework [7–9] has been particularly successful in describing 1D systems and their properties such as universal power-law scaling in 1D arrays [10–13] as well as spin-charge separation [14, 15] and charge fractionalization [16] in tunnel-coupled 1D wires.

However, quantum transport in Coulomb-coupled TLLs is not as well established. When two conductors are placed in close proximity, current sourced in the active conductor can induce a voltage in the passive conductor through Coulomb interactions, as shown in Fig. 1(a). This phenomenon, called Coulomb drag, has historically been understood in terms of momentum transfer (MT) between the active and the passive circuit charge carriers [17–19], but can also be interpreted as a charge rectification of energy fluctuations by the passive circuit [20]. Both interpretations yield comparable results for weak electronic interlayer correlations and crucially rely on the presence of an intrinsic electron-hole asymmetry, preventing the cancellation of electron-electron and electron-hole contributions [20]. The strong electronic correlations inherent to TLLs break down this equivalence, and both the MT approach [21–24] and the CR approach [25, 26] yield different predictions for 1D Coulomb drag. Notably,

the drag voltage polarity is independent of the drive current direction in the CR framework while charge carriers are displaced in the direction of the current flow in the MT framework. In 1D drag experiments, a broad range of results have been obtained, some consistent with an MT framework [27–29], some with a CR framework [30, 31] and others arising in the presence more exotic 1D states [32–34]. A clear characterization of the relative strength of these various drag-inducing paradigms remains lacking however.

In this work, we report Coulomb drag measurements between 1D quantum wires in a vertically-coupled architecture [28, 29] with simultaneous contributions from both MT and CR, allowing a clear comparison between these two drag-inducing paradigms. The relative strength of both contributions is tunable with both gate voltage and temperature. We conduct a systematic temperature-dependence analysis of Coulomb drag and observe an upturn behavior at numerous gate positions. The functional shape of the temperature-dependent signals appears to follow either a power-law or an Arrhenius dependence, as typically predicted in 1D systems with strong electron interactions [21, 24, 31, 35–37]. These results are contrasted with measurements in laterally-coupled quantum wires [31] to highlight the role of interwire separation in the onset of this control.

II. Device operation and wires characterization

A schematic of the vertically-coupled quantum wires device used in this work is shown in Fig. 1(b), with an optical image provided in Supplementary section 1. As the two wires are defined in two separate quantum wells, they are only separated by a 15 nm-wide hard AlGaAs barrier grown by molecular beam epitaxy, resulting in an interwire separation $d_{vert} = 33$ nm. Each wire is defined by a

* Email of Author to whom correspondence should be addressed: dlaroc10@ufl.edu

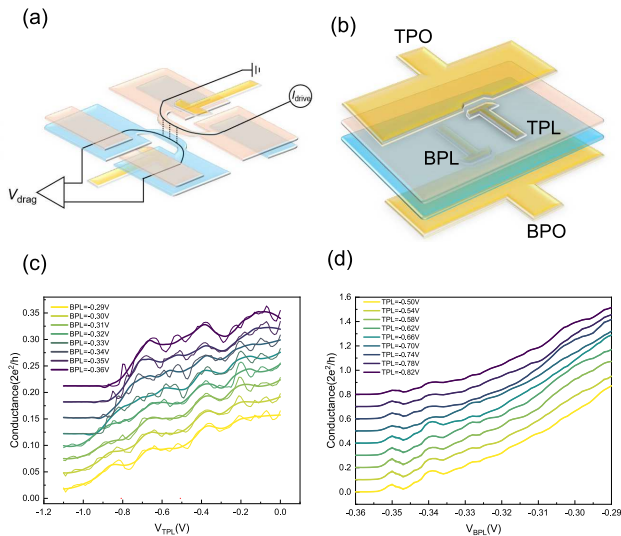


FIG. 1. Design of the vertically integrated quantum wire device. (a) Schematic of a 1D Coulomb drag measurement in vertically-coupled quantum wires defined electrostatically. The conducting part of the top layer is shown in pink and that of the bottom layer is shown in blue. (b) Schematic of the active part of the double quantum wire device. Each wire consists of a plunger (PL) and a pinch-off (PO) gate. The PO gates are primarily used to independently contact the quantum wires and minimize tunneling current between them, while the PL gates are used to adjust the wire’s width and electronic density, similar to previous work in vertically-coupled quantum wires [28, 29]. In the interacting region of the device, two vertically-superimposed independent quantum wires are created, leveraging selective layer depletion with the PO gates. (c) Top (drive) wire conductance as a function of the top (drive) and bottom (drag) gate voltages. Interwire crosstalk is only visible on the lower end of the top wire gating range. Plateau-like features are clearly visible in the smoothed data (thick line). Successive line-cuts are vertically offset by 0.03 ($2e^2/h$) for visibility, with the lowest BPL value at the bottom. (d) Bottom (drag) wire conductance as a function of the bottom (drag) and top (drive) gate voltages. Interwire crosstalk is negligible compared to the top (drive) wire. Successive line-cuts are vertically offset by 0.1 ($2e^2/h$) for visibility purposes, with the lowest BPL value at the bottom. In both wires, the conductance plateaus are not quantized at integer values of $2e^2/h$ as the wires are non-ballistic.

pinch-off (PO) gate and a plunger (PL) gate. Fig. 1(a) shows the conducting region of the device when appropriate negative voltages are applied to all four gates, creating two independently contacted quantum wires. Crucially, this design allows for interlayer interactions only in the region where the two quasi-1D wires overlap. The conductance of the top wire as a function of the top PL gate for different bottom PL gate voltages is displayed in Fig. 1(c). The 1D subband plateau-like features are prominently visible in the smoothed data, while the raw data still reveals the presence of resonances, likely due to disorder-induced quantum dots. It is worth noting

that limited cross-talk is observed between the bottom PL gate and the top wire. However, the subband position of the bottom wire does not show such crosstalk, as depicted in Fig. 1(d). The bottom wire exhibits sharper subbands and fewer defects compared to the top wire, and is notably less resistive. Therefore, in subsequent Coulomb drag measurements, we utilize the top wire as the drive wire and the bottom wire as the drag wire, as the drag signal is more dependent on the drag wire quality. Coulomb drag measurements with the bottom wire as the drive wire are presented in Supplementary section 3.

III. Coulomb drag measurements

First, we investigate the subband dependence of the drag signal at the base temperature of the cryostat, with an electron temperature below 15 mK. Fig. 2(a) and Fig. 2(b) present the Coulomb drag mapping as a function of both TPL and BPL gate voltage. In this measurement, the drag signal is recorded using two different drive current directions: Fig. 2(a) displays the drag signal V_{drag}^R when the drive current direction aligns with the drag voltage direction, while Fig. 2(b) shows V_{drag}^L when the drive current direction is reversed. Clear vertical stripes corresponding to the drag wire subband positions are observed in both directions. Additionally, the drag signal exhibits sign changes at various positions, consistent with prior experiments [28, 31]. Alongside the vertical stripes, sloped stripes are observed, corresponding to constant density lines of the drive wire. To investigate the mechanisms of both CR and MT, we extract the symmetric component, $V_{drag}^S = \frac{V_{drag}^R + V_{drag}^L}{2}$, and the antisymmetric component $V_{drag}^{AS} = \frac{V_{drag}^R - V_{drag}^L}{2}$. As the CR component’s polarity remains unchanged upon reversing the drive current direction, it is given by the symmetric contribution while the antisymmetric component represents the MT contribution. To assess the relative strengths of these components, we plot in Fig. 2(c) the 2D map of the ratio between the symmetric and antisymmetric components, $r_{SAS} = \frac{V_{drag}^S + \Gamma}{V_{drag}^{AS} + \Gamma}$. Here an offset Γ , comparable to the measurement noise, is added to the ratio to distinguish nearly null signals (ratio near 1) from signals where the antisymmetric component is strongest (ratio near 0). At base temperature, the CR component (ratio larger than 2) dominates most gate-space regions with a few notable exceptions where MT is the primary contribution. However, the antisymmetric component dominates across the entire map at approximately 800 mK as shown in Fig. 2(d), providing clear evidence of the distinct temperature dependence of the two components. We also measured the two contributions to the drag signal in a lateral device, wherein the two wires are defined in a single quantum well and separated by a 150 nm-wide gate-defined potential barrier, resulting in an interwire

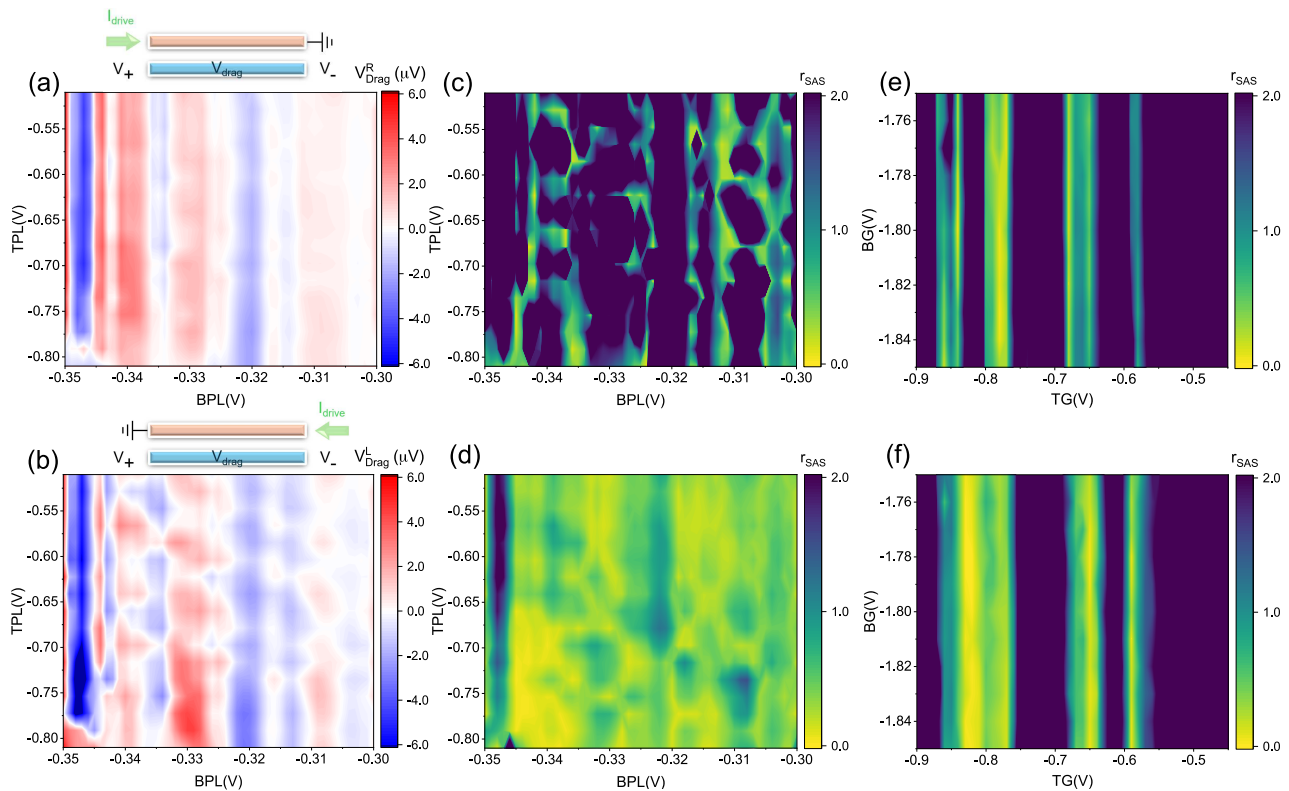


FIG. 2. Rectified drag of the quantum wires. (a) Drag voltage as a function of the top (drive) and bottom (drag) gate voltages when the drive current is in the same direction as the drag voltage measurement. The measurement was performed at the cryostat base electron temperature, below 7 mK. (b) Same as (a), but with the drive current direction reversed. (c,d) Ratio between symmetric and antisymmetric components (see text) of the vertically-coupled device at the cryostat base electron temperature (c) and at 800 mK (d). An offset Γ , comparable to the measurement noise, is added to the ratio to distinguish nearly null signals (ratio of 1) from signals with a strong antisymmetric component. (e,f) r_{SAS} as a function of the bottom (drive) gate and top (drag) gate voltages for laterally-coupled quantum wires at (e) 100 mK and (f) 800 mK.

separation $d_{lat} \geq 250$ nm. Fig. 2(e) and Fig. 2(f) illustrate the ratio 2D map at base temperature (electron temperature around 100 mK) and 800 mK. In the lateral device, the MT component exhibits fewer regions of dominance, with their range only expanding slightly at 800 mK. Thus, both vertically and laterally-coupled devices demonstrate tunable contributions of Coulomb drag through gate and temperature adjustments, but that tunability is notably stronger in vertically-coupled devices with a smaller interwire separation.

This tunability of the two contributions to Coulomb drag in vertically-coupled wires enables us to study their temperature dependence individually and simultaneously on the same device. We present such a study in Fig. 3 for a constant drive wire density, selected to be at $TPL = -0.735$ V. Similar results extracted at different TPL values and at fixed BPL are presented in Supplementary section 5, and yield qualitatively similar results. Fig. 3(a) and Fig. 3(b) illustrate the BPL gate-temperature 2D plots for the symmetric and antisymmetric components, respectively. Their ratio is presented in Fig. 3(c). Two distinct temperature regimes can be identified: a low-temperature regime below ~ 1.5 K where both compo-

nents exhibit BPL gate tunable sign changes in the drag voltage polarity and a high-temperature regime where the drag signal is strictly positive, increases with increasing temperature and is dominated by the antisymmetric component. In the low-temperature regime, the sign change of V_{drag}^S overlaps the onset of drag wire subbands (see Supplementary section 4), while V_{drag}^{AS} is primarily positive, with only a few regions with negative V_{drag}^{AS} and no clear correlation to the 1D wire subbands. The polarity change of V_{drag}^S is expected within the CR model for Coulomb drag [26], and has recently been previously reported in quantum wires [31]. However, standard MT theories [21, 22, 24] predict a negative drag voltage (or a positive drag resistance R_{drag}), as observed in early 1D Coulomb drag experiments [27, 29] and in contrast with the results reported here. While unexpected in clean systems, such an MT induced negative drag resistance has been predicted to occur in disordered systems, either in the non-linear regime away from equilibrium [37], through lattice relaxations in the hopping regime [38], through Umklapp scattering in helical edges [34, 36] and in the presence of a single quantum dot in one of the wires [39].

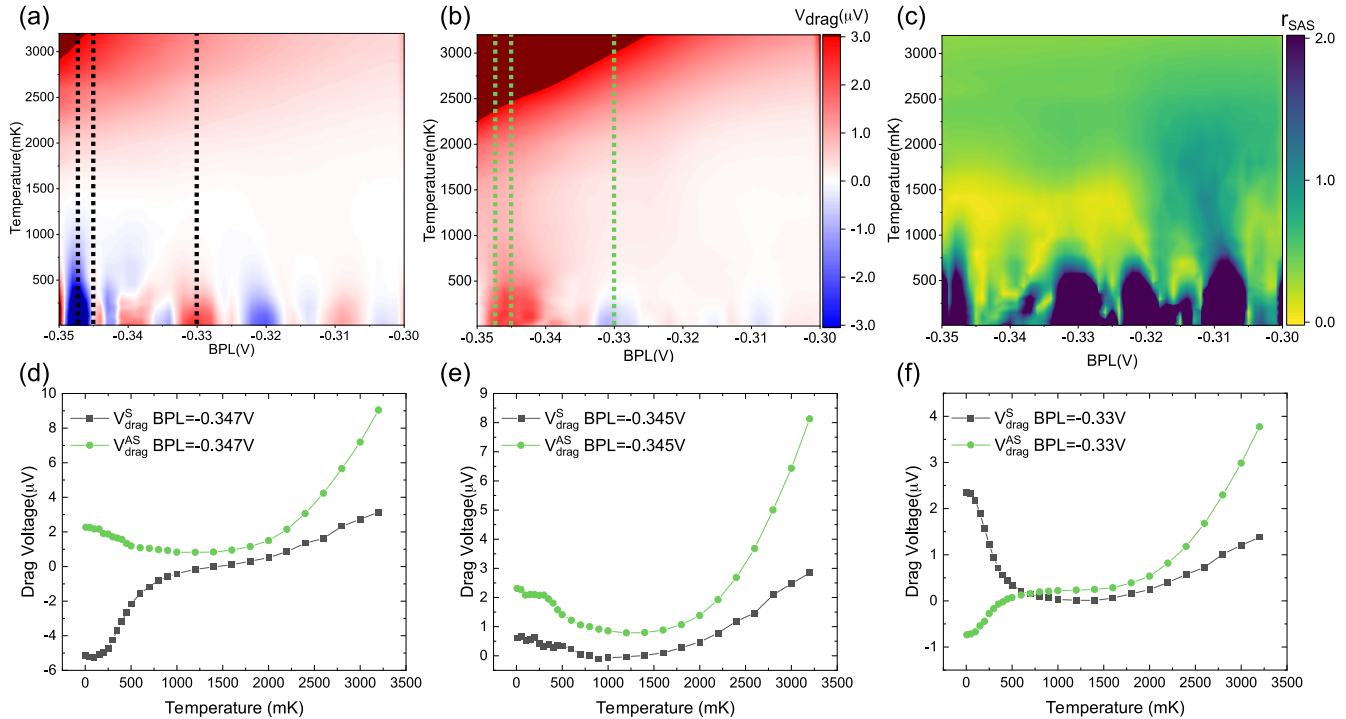


FIG. 3. Gate and temperature tunable rectified drag. (a,b) BPL gate-temperature 2D plot at TPL=-0.735V of (a) the symmetric component and (b) the antisymmetric component. (c) The ratio between the symmetric and the antisymmetric components, r_{SAS} , as a function of BPL gate voltage and temperature. Above ~ 750 mK, the drag signal is dominated by the antisymmetric component. (d,e,f) The symmetric and antisymmetric component as a function of the temperature at (d) TPL=-0.347V, (e) TPL=-0.345V and (f) TPL=-0.33V.

The transition between both regimes is characterized by an upturn in the magnitude of the drag signal in the vicinity of $T \sim 1.5$ K, both for symmetric and antisymmetric contributions. This transition is more easily visible in Fig. 3(d-f), where V_{drag}^S and V_{drag}^{AS} are presented at different TPL values. Such an upturn had been previously predicted to occur due to the creation of a charge-density wave for positive drag resistance occurring through backscattering [21, 35], albeit at much lower temperatures, in the spin-incoherent regime [23] or for negative drag arising from Umklapp scattering [36]. However, as this upturn occurs at the same temperature for both the MT and the CR contribution and for virtually all drag and drive wire densities, it is unlikely that the aforementioned models accurately describe this observation. In a typical quantum wire, 1D subbands typically become smeared out and non-visible through conductance measurements around $T \sim 1.5$ K, where the typical subband energy spacing becomes comparable to the temperature [40]. Combined with the disappearance of the subband structure in the reported Coulomb drag data above the upturn temperature, it is likely that the transition between the high and the low-temperature drag regimes arises from a fundamental change in the drag-inducing scattering mechanisms between separated and

temperature-mixed 1D subbands.

IV. Coulomb drag high-temperature regime

Looking at r_{SAS} presented in Fig. 3(c), it is clear that the antisymmetric drag component becomes the leading contribution to drag at temperatures above ~ 800 mK. This indicates a fundamental difference in the temperature dependence of CR- and MT-induced drag. To elucidate this temperature dependence further, we analyzed the functional shape of the Coulomb drag temperature dependence. Both contributions are well-described by a power-law ($V_{drag} \propto A \times T^B$), in qualitative agreements with numerous theoretical models for 1D Coulomb drag at elevated temperatures [21, 23, 37].

The parameters extracted from a power-law fit over the linear range in the log-log plot for four line cuts at TPL=-0.5475V, TPL=-0.6225V, TPL=-0.6788V, and TPL=-0.735V, are presented in Fig. 4(c), Fig. 4(d), Fig. 4(e), and Fig. 4(f) respectively, along with typical examples of the temperature dependence of the drag signal in log-log plot in Fig. 4(a) and 4(b). The power-law exponent of both components oscillates with changes in the BPL gate. This result is expected as, in 1D, the value of

this exponent is predicted to depend on the strength of electron-electron interactions, which depend themselves on the wires' electronic density [21]. Similar oscillations are also observed in the drag magnitude. These gate-dependent peaks align with theoretical predictions that the Coulomb drag signal is enhanced upon the opening of 1D subbands.

For most gate positions, the power-law exponent of the antisymmetric component, ranging from 3 to 5, exceeds that of the symmetric component, ranging from 2.5 to 4. The power-law exponent from the symmetric contribution exhibits minimal wire subband dependence, but is notably different from the quadratic dependence predicted in non-interacting models [26]. Additional theoretical work will be required to see if electron interactions, small inter-wire separation, and disorder can result in such power-law exponents. Theoretical calculations for MT-induced 1D drag predict $B = 2K_c - 1$ [21] or $B = -4K_c - 3$ [36] or, for non-identical wires specifically, density-independent power-law exponents of relatively large value, $B = 5$ [22] or $B = 4$ [41]. Here, K_c is the Luttinger parameter of relative charge mode [21].

Neither model appears to appropriately reflect our data. The interaction-dependent results lead to $K_c > 1$, a value inconsistent with repulsive interactions. However, the density-dependent results do not reflect the fact that the extracted power-law exponents exhibit a density dependence. Models for Coulomb drag between two spin-incoherent TLLs [23] predict a power-law exponent of $8K_C - 3$ in the high-temperature regime when the Fermi energy is higher than the spin exchange energy. While this model would yield a Luttinger interaction parameter of $K_c = 0.875$ for $B = 4$, consistent with repulsive electron-electron interactions, this model is only applicable at low electron density where $na_B < 1$. Here n is the 1D electron density and $a_B = 10.2nm$ is the GaAs Bohr radius. From our estimates, such a low density can only be achieved in the single subband regime, and this model cannot readily explain the large density-dependent power-law exponents observed in our devices. This highlights the need for more theoretical work to grasp the richness of Coulomb drag between multi-channel quantum wires away from the ballistic regime.

Looking at the power-law magnitude, both the symmetric and antisymmetric components increase as the electron density decreases, consistent with enhanced interaction strength and reduced screening at lower electron density. Notably, this dependence is well-fitted by a linear slope going over small density oscillations, as shown by the solid lines in Fig. 4(c-f). The slopes for the symmetric component are -14.3, -11.7, -17.2, and -19.9 for the four line cuts respectively, while the ones for the antisymmetric components are -24.6, -28.6, -37.5, and -33.3. The ratio between these slopes, r_{int} , is presented in the inset of Fig. 4(f). In the high-temperature regime where the 1D subband density of state is notably smeared, it is reasonable to assume that the quasi-1D density, and hence k_f , varies linearly with plunger gate

voltage, similarly to what happens in 2D systems [42]. As such, the linear increase of the drag magnitude in a log-log plot implies an exponential dependence of the drag signal upon k_f . This is in good agreement with standard prediction for 1D Coulomb drag where the drag magnitude $\lambda_{AS} \sim e^{-2k_f d}$ [19]. Since the ratios r_{int} are in the vicinity of 2, it implies that the CR Coulomb drag magnitude $\lambda_S \sim e^{-k_f d}$. The stronger $k_f d$ dependence of MT-induced Coulomb drag thus explains why CR Coulomb drag remains dominant at high temperatures in laterally coupled devices as the nearly 6 times larger interwire separation renders the MT contribution negligible, even at elevated temperatures. We note that other theoretical models [24, 35, 43] predict an Arrhenius temperature dependence of the Coulomb drag signal ($V_{drag} \propto \alpha e^{(\frac{\beta}{T})}$). In contrast to the aforementioned theories, the result of such an analysis, presented in Supplementary section 7, shows negligible k_f dependence and is not further discussed.

V. Coulomb drag low-temperature regime

In the low-temperature regime, both the MT and the CR components (see Fig. 3) show typical TLL behavior of an increasing drag voltage magnitude with decreasing temperature over a wide range of gate voltages. As shown in Fig. 5, the low-temperature data is fitted to both a power-law and an Arrhenius dependence for 2 nA and 9 nA. In Fig. 5(a), the antisymmetric power-law fitting parameters are presented at different drag and drive wire densities for a 2nA drag current. The power-law exponents are generally negative, implying an increasing drag magnitude with decreasing temperature. At low and large drag subband occupancies, the power-law exponent averages 0.5 across numerous data points. As such, it appears that the wires Fermi wavevectors have little incidence on the shape of the temperature dependence. However, for intermediate drag wire densities $\sim -0.335 < V_{BPL} < -0.317$, the power-law exponent becomes positive for $V_{TPL} = -0.5475V$ and $V_{TPL} = -0.735V$ while it goes to a value near $B \sim -1$ for $V_{TPL} = -0.6225V$. The observation of negative power-law exponents coincides with the opening of 1D subbands in either wire, while the positive one coincides with the closing of 1D subbands, or the occurrence of conductance plateaus. This dependence is more clearly seen by looking at the derivative of V_{drag} temperature dependence, as shown in Supplementary section 7. That rich temperature dependence of the MT-induced drag in the multi-channel disordered regime, both in terms of temperature dependence and magnitude, highlights the need for further theoretical work on the subject. The antisymmetric drag magnitude still appears to follow an exponential dependence of $k_f d$, as seen from the linear dependence of the power-law intercept with gate voltage.

Fig. 5(b) shows the results of the Arrhenius fit at 2nA. In this low-temperature regime, the Arrhenius param-

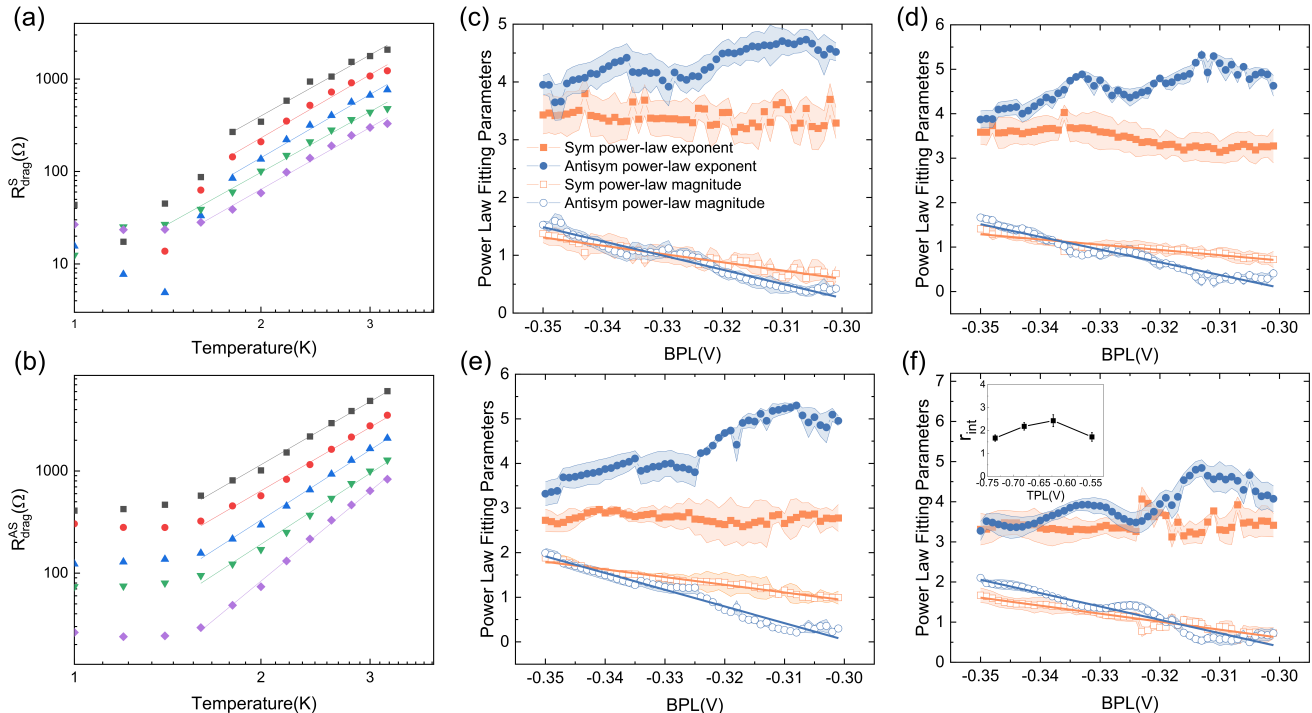


FIG. 4. High-temperature line cut analysis. (a,b) Log-log plot and power-law fitting for TPL= -0.735V for (a), the symmetric component and (b) the antisymmetric component. From top to bottom, the BPL gate voltages are -0.35V , -0.34V , -0.33V , -0.32V and -0.31V . The linearity of R_{drag} in a log-log plot for $1.6\text{K} \lesssim T \lesssim 3.2\text{K}$ confirms the power-law nature of the temperature dependence. (c-f) Power-law fitting results for the power-law exponent (full symbols) and magnitude (open symbols) at line cuts of (c) TPL= -0.5475V , (d) TPL= -0.6225V , (e) TPL= -0.6788V and (f) TPL= -0.735V for the symmetric (orange squares) and the antisymmetric (blue circles) components. The magnitude as a function of the BPL gate voltage has been linearly fitted. The error bars, arising from the end point selection in the fitting procedure, are shown as light shading. See Supplementary section 6 for more details. Inset of (f): Ratio r_{int} between the slopes of the symmetric and antisymmetric magnitudes. The errors on this data were calculated using a bootstrap Monte Carlo method. See Supplementary section 9 for more details.

ters exhibit a dependence on gate voltage, and as such are not inconsistent with MT theories [24, 35, 43]. In a qualitatively similar fashion to the power-law fits, drastic changes between the value of β , both in position and magnitude, occur depending on whether a 1D subband is opening or closing, once again highlighting the need for further theoretical work in the field. We note that the relatively small temperature range of the monotonic temperature dependence in the low-temperature regime combined with the lack of clear theoretical predictions makes it virtually impossible to establish the functional form of the temperature dependence. Owing to the relative weakness of the symmetric drag signal near the upturn point at 2 nA, we were not able to reliably fit a power-law function for a significant number of gate-voltage values. As such, we instead extract the power-law exponents for both the symmetric and the antisymmetric component for drive current values of 9 nA, as presented in Fig. 5(c) and (d) respectively. The Arrhenius fitting results, being overly noisy, are shown in Supplementary section 6. The symmetric components' power-law exponent shows a constant evolution within a single subband, decreasing with

increasing electron density increases within each individual subband. This result is notably different from the predicted value of $B = -1$ for multi-channel Luttinger liquids in the diffusive regime[31]. The MT power-law fits presented in Fig. 5(d) are in relatively good agreement with the results presented in Fig. 5(a), despite exhibiting a larger power-law exponent spread. This larger spread is attributed to the reduced range with a meaningful temperature dependence, arising from heating effects.

VI. Discussion

Overall, our study successfully demonstrated the gate and temperature tunability of CR and MT Coulomb drag contributions while contrasting their density and temperature dependence. Interestingly, both components exhibited positive and negative polarities at temperatures below 500 mK, with the CR component changing sign whenever the subband number changed. Notably, the observation of a negative MT component of the drag signal sits at odd with Coulomb drag prediction in clean

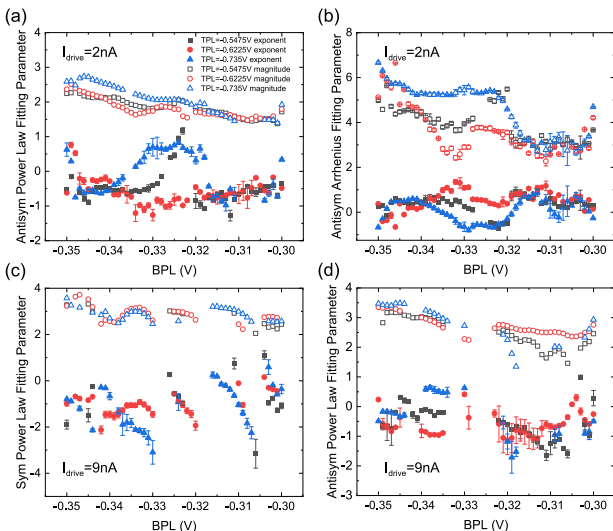


FIG. 5. Low-temperature Coulomb drag analysis. Extracted power-law and Arrhenius fitting parameters include exponent (solid symbols) and magnitude (open symbols) in the temperature range 0.1K to 1.4K for TPL=-0.735V (black), TPL=-0.6225V (red), and TPL=-0.5475V (blue). (a) Power-law fitting results of the antisymmetric component when the drive current is 2nA. (b) Arrhenius fitting results of the antisymmetric component when the drive current is 2nA. (c) Symmetric component power-law fitting results when the drive current is 9nA. (d) Antisymmetric component power-law fitting results when the drive current is 9nA. Data points with high error bars, coinciding with subband boundaries where the CR-induced drag signal was comparable to the noise, are omitted, resulting in gaps in the data. Error bars smaller than the symbol size have also been omitted. The error bars have been calculated similarly to those for Fig. 4.

TLLs [21, 22, 24] and highlights the role of disorder in our system, and its impact on the nature of Coulomb scattering. While a number of observations such as a temperature upturn in the drag signal strength and an increasing drag magnitude with decreasing temperature are consistent with Luttinger liquid physics, the specific values of the power-law exponents extracted are not readily explained within the current Coulomb drag literature. Our observations highlight the richness of interactions between Coulomb-coupled 1D systems and the need for further theoretical investigations, especially in the presence of disorder. Such studies could be instrumental to the realization of novel applications in the realm of topological quantum computing [1] or heat harvesting [3].

VII. Methods

Material growth and device fabrication The wires were patterned on an n-doped GaAs/AlGaAs electron bilayer heterostructure with two 18-nm-wide quantum wells separated by a 15-nm-wide $\text{Al}_{0.3}\text{Ga}_{0.7}\text{As}$ barrier. The unpatterned density and mobility of the

GaAs quantum well are $n = 2.98 \times 10^{11} \text{ cm}^{-2}$ and $\mu = 7.4 \times 10^4 \text{ cm}^2/\text{V} \cdot \text{s}$, respectively. After a mesa-structure was wet-etched using phosphoric acid, Ge-Au-Ni-Au ohmic contacts were deposited on the structure and annealed at 420° for 60 s. A set of two Ti-Au split gates was then defined on the surface of the heterostructure, using electron-beam lithography [Fig. 1(a)]. Once the upper side processing was complete, bare GaAs was epoxied on top of the heterostructure and the sample flipped, mechanically lapped and chemically etched using subsequent citric and hydrofluoric mixtures until the lower 2DEG was only $\sim 150 \text{ nm}$ away from the lower surface (now on top of the device), following the EBASE technique [44]. To ensure that no off-mesa leakage occurred between the bottom and top gates, a thin 40 nm layer of Al_2O_3 was deposited on the new surface using atomic layer deposition. Using phosphoric acid, vias were then etched through the surface to enable electrical connection to the ohmic contacts and the split gates buried under the surface of the device. Finally, using electron-beam lithography, another set of Ti-Au split gates was defined on the top side of the device, and aligned with the bottom gates. The end result is depicted in Fig. 1(a), with an optical image provided in Supplementary section 1.

Measurement techniques

Transport measurements were performed in a dilution refrigerator (LD250, Bluefors) with a base temperature less than 7 mK. The device was mounted in an experimental cell, which is thermally anchored to the mixing chamber of the dilution refrigerator. The polycarbonate cell is then filled with liquid Helium-3. The liquid is thermalized to the mixing chamber of a dilution refrigerator via annealed silver rods that enter the Helium-3 cell. These bring the system's base temperature near that of the dilution unit, below 15 mK. All measurements were performed in an ultraquiet environment, shielded from electromagnetic noise. RC filters with cutoff frequencies of 50 kHz were employed to reduce RF heating. All measurements were performed using standard low-frequency lock-in amplification techniques. Additionally, source-measure units were used to source and measure DC signals applied to the electrostatic gates. Transport measurements on individual quantum wires were performed at base temperature using a constant 100 μV excitation at 13 Hz in both wires in a two-contact configuration. The Coulomb drag measurements were performed in a constant-current mode where a typical 2 nA current was sent at 13 Hz through the drive wire. Some measurements were performed with a larger current, up to 9 nA. In this configuration, the out-of-phase current was always much smaller than the in-phase current. The tunneling measurements, as shown in Supplementary section 2, were performed by sending a small source-drain voltage across the device for different top PO gate and bottom PO gate values. The combination was selected such that the tunneling

resistance between the two wires was larger than $10M\Omega$ in a bias range of $\pm 1.5mV$. Detailed configuration of the drag measurement is also presented in Supplementary section 2.

Supplementary information

Supplementary information is available

Acknowledgements

This work was performed, in part, at the Center for Integrated Nanotechnologies, an Office of Science User Facility operated for the U.S. Department of Energy (DOE) Office of Science. Sandia National Laboratories is a multimission laboratory managed and operated by National Technology & Engineering Solutions of Sandia, LLC, a wholly owned subsidiary of Honeywell Inter-

national, Inc., for the U.S. DOE's National Nuclear Security Administration under contract DE-NA-0003525. The views expressed in the article do not necessarily represent the views of the U.S. DOE or the United States Government. Part of this work was conducted at the Research Service Centers of the Herbert Wertheim College of Engineering at the University of Florida. A portion of this work was also performed at the National High Magnetic Field Laboratory. This work was partially supported by the National High Magnetic Field Laboratory through the NHMFL User Collaboration Grants Program (UCGP). The National High Magnetic Field Laboratory is supported by the National Science Foundation through NSF/DMR-1644779 and the State of Florida. Finally, we also acknowledge Alex Levchenko for enlightening discussions.

-
- [1] R. M. Lutchyn, E. P. A. M. Bakkers, L. P. Kouwenhoven, P. Krogstrup, C. M. Marcus, and Y. Oreg, Majorana zero modes in superconductor–semiconductor heterostructures, *Nature Reviews Materials* **3**, 52 (2018).
- [2] K. Flensberg, F. von Oppen, and A. Stern, Engineered platforms for topological superconductivity and majorana zero modes, *Nature Review Materials*, 944 (2021).
- [3] B. Sothmann, R. Sánchez, and A. N. Jordan, Thermoelectric energy harvesting with quantum dots, *Nanotechnology* **26**, 032001 (2014).
- [4] B. Bhandari, G. Chiriacò, P. A. Erdman, R. Fazio, and F. Taddei, Thermal drag in electronic conductors, *Physical Review B* **98**, 035415 (2018).
- [5] J. Voit, One-dimensional Fermi liquids, *Reports on Progress in Physics* **58**, 977 (1995).
- [6] A. Imambekov and L. I. Glazman, Universal Theory of Nonlinear Luttinger Liquids, *Science* **323**, 228 (2009).
- [7] S. Tomonaga, Remarks on Bloch's method of sound waves applied to many-fermion problems, *Progress of Theoretical Physics* **5**, 544 (1950).
- [8] J. M. Luttinger, An Exactly Soluble Model of a Many-Fermion System, *Journal of Mathematical Physics* **4**, 1154 (1963).
- [9] F. D. M. Haldane, Effective Harmonic-Fluid Approach to Low-Energy Properties of One-Dimensional Quantum Fluids, *Physical Review Letters* **47**, 1840 (1981).
- [10] S. Tarucha, T. Honda, and T. Saku, Reduction of quantized conductance at low temperatures observed in 2 to 10 μm -long quantum wires, *Solid State Communications* **94**, 413 (1995).
- [11] M. Bockrath, D. H. Cobden, J. Lu, A. G. Rinzler, R. E. Smalley, L. Balents, and P. L. McEuen, Luttinger-liquid behaviour in carbon nanotubes, *Nature* **397**, 598 (1999).
- [12] Y. Sato, S. Matsuo, C.-H. Hsu, P. Stano, K. Ueda, Y. Takeshige, H. Kamata, J. S. Lee, B. Shojaei, K. Wickramasinghe, J. Shabani, C. Palmstrom, Y. Tokura, D. Loss, and S. Tarucha, Strong electron-electron interactions of a Tomonaga-Luttinger liquid observed in InAs quantum wires, *Physical Review B* **99**, 155304 (2019).
- [13] P. Wang, G. Yu, Y. H. Kwan, Y. Jia, S. Lei, S. Klemenz, F. A. Cevallos, R. Singha, T. Devakul, K. Watanabe, T. Taniguchi, S. L. Sondhi, R. J. Cava, L. M. Schoop, S. A. Parameswaran, and S. Wu, One-dimensional Luttinger liquids in a two-dimensional moiré lattice, *Nature* **605**, 57 (2022).
- [14] O. M. Auslaender, H. Steinberg, A. Yacoby, Y. Tserkovnyak, B. I. Halperin, K. W. Baldwin, L. N. Pfeiffer, and K. W. West, Spin-Charge Separation and Localization in One Dimension, *Science* **308**, 88 (2005).
- [15] Y. Jompol, C. J. B. Ford, J. P. Griffiths, I. Farrer, G. A. C. Jones, D. Anderson, D. A. Ritchie, T. W. Silk, and A. J. Schofield, Probing Spin-Charge Separation in a Tomonaga-Luttinger Liquid, *Science* **325**, 597 (2009).
- [16] H. Steinberg, G. Barak, A. Yacoby, L. N. Pfeiffer, K. W. West, B. I. Halperin, and K. Le Hur, Charge fractionalization in quantum wires, *Nature Physics* **4**, 116 (2008).
- [17] M. B. Pogrebinskii, Mutual drag of carriers in a semiconductor-insulator-semiconductor system, *Soviet Physics-Semiconductors* **11**, 372 (1977).
- [18] T. J. Gramila, J. P. Eisenstein, A. H. MacDonald, L. N. Pfeiffer, and K. W. West, Mutual friction between parallel two-dimensional electron systems, *Physical Review Letters* **66**, 1216 (1991).
- [19] B. N. Narozhny and A. Levchenko, Coulomb drag, *Reviews of Modern Physics* **88**, 025003 (2016).
- [20] A. Kamenev and Y. Oreg, Coulomb drag in normal metals and superconductors: Diagrammatic approach, *Physical Review B* **52**, 7516 (1995).
- [21] R. Klesse and A. Stern, Coulomb drag between quantum wires, *Physical Review B* **62**, 16912 (2000).
- [22] M. Pustilnik, E. G. Mishchenko, L. I. Glazman, and A. V. Andreev, Coulomb Drag by Small Momentum Transfer between Quantum Wires, *Physical Review Letters* **91**, 126805 (2003).
- [23] G. A. Fiete, K. Le Hur, and L. Balents, Coulomb drag between two spin-incoherent Luttinger liquids, *Physical Review B* **73**, 165104 (2006).
- [24] A. P. Dmitriev, I. V. Gornyi, and D. G. Polyakov, Coulomb drag between ballistic quantum wires, *Physical Review B* **86**, 245402 (2012).
- [25] Y. V. Nazarov and D. V. Averin, Current Drag in Capacitively Coupled Luttinger Constrictions, *Physical Review Letters* **81**, 653 (1998).
- [26] A. Levchenko and A. Kamenev,

- Coulomb Drag in Quantum Circuits, *Physical Review Letters* **101**, 216806 (2008).
- [27] P. Debray, V. Zverev, O. Raichev, R. Klesse, P. Vasilopoulos, and R. S. Newrock, Experimental studies of Coulomb drag between ballistic quantum wires, *Journal of Physics: Condensed Matter* **13**, 3389 (2001).
- [28] D. Laroche, G. Gervais, M. P. Lilly, and J. L. Reno, Positive and negative Coulomb drag in vertically integrated one-dimensional quantum wires, *Nature Nanotechnology* **6**, 793 (2011).
- [29] D. Laroche, G. Gervais, M. P. Lilly, and J. L. Reno, 1D-1D Coulomb Drag Signature of a Luttinger Liquid, *Science* **343**, 631 (2014).
- [30] L. Anderson, A. Cheng, T. Taniguchi, K. Watanabe, and P. Kim, Coulomb drag between a carbon nanotube and monolayer graphene, *Physical Review Letters* **127**, 257701 (2021).
- [31] R. Makaju, H. Kassar, S. M. Daloglu, A. Huynh, D. Laroche, A. Levchenko, and S. J. Addamane, Nonreciprocal coulomb drag between quantum wires in the quasi-one-dimensional regime, *Phys. Rev. B* **109**, 085101 (2024).
- [32] M. Yamamoto, M. Stopa, Y. Tokura, Y. Hirayama, and S. Tarucha, Negative Coulomb Drag in a One-Dimensional Wire, *Science* **313**, 204 (2006).
- [33] S. M. Tabatabaei, D. Sánchez, A. L. Yeyati, and R. Sánchez, Andreev-coulomb drag in coupled quantum dots, *Physical Review Letters* **125**, 247701 (2020).
- [34] L. Du, J. Zheng, Y.-Z. Chou, J. Zhang, X. Wu, G. Sullivan, A. Ikhlassi, and R.-R. Du, Coulomb drag in topological wires separated by an air gap, *Nature Electronics* **4**, 573 (2021).
- [35] T. Fuchs, R. Klesse, and A. Stern, Coulomb drag between quantum wires with different electron densities, *Physical Review B* **71**, 045321 (2005).
- [36] Y.-Z. Chou, Localization-driven correlated states of two isolated interacting helical edges, *Physical Review B* **99**, 045125 (2019).
- [37] C. Zhou and H. Guo, Coulomb drag between quantum wires: A nonequilibrium many-body approach, *Physical Review B* **99**, 035423 (2019).
- [38] D. Liu, J. Wang, C. Bi, M. Li, N. Lu, Z. Chen, and L. Li, Lattice relaxation forward negative coulomb drag in hopping regime, *Electronics* **11**, 1273 (2022).
- [39] M. Shimizu, M. Yamamoto, M. Stopa, M. Honda, and S. Tarucha, Negative coulomb drag in coupled wire and quantum dot system, *Physica E: Low-dimensional Systems and Nanostructures* **26**, 460 (2005).
- [40] K. J. Thomas, J. T. Nicholls, N. J. Appleyard, M. Y. Simmons, M. Pepper, D. R. Mace, W. R. Tribe, and D. A. Ritchie, Interaction effects in a one-dimensional constriction, *Physical Review B* **58**, 4846 (1998).
- [41] R. G. Pereira and E. Sela, Spin-charge coupling in quantum wires at zero magnetic field, *Physical Review B* **82**, 115324 (2010).
- [42] D. Chen, S. Cai, N.-W. Hsu, S.-H. Huang, Y. Chuang, E. Nielsen, J.-Y. Li, C. W. Liu, T. M. Lu, and D. Laroche, Density dependence of the excitation gaps in an undoped si/sige double-quantum-well heterostructure, *Applied Physics Letters* **119**, 10.1063/5.0068538 (2021).
- [43] A. P. Dmitriev, I. V. Gornyi, and D. G. Polyakov, Ultranarrow resonance in Coulomb drag between quantum wires at coinciding densities, *Physical Review B* **94**, 085404 (2016).
- [44] M. V. Weckwerth, J. A. Simmons, N. E. Harff, M. E. Sherwin, M. A. Blount, W. E. Baca, and H. C. Chui, Epoxy bond and stop-etch (EBASE) technique enabling backside processing of (Al)GaAs heterostructures, Superlattices and Microstructures **20**, 561 (1996).